Article

Epitaxy of Monoclinic VO$_2$ on Large-Misfit 3*m* Template Enabled by a Metastable Interfacial Layer

Zhiwei Zhang, Xingxing Li,* Yong Cheng, Bo Li, Jinliang Wu, Ling Zhang, Zhigang Yin,* and Xingwang Zhang

Read Online

| ACCESS | | Metrics & More | | Article Recommendations | | Supporting Information |

ABSTRACT: We report the epitaxial growth of a monoclinic VO$_2$ thin film on the CoFe$_2$O$_4$(111) template, assisted by an interfacial layer of the metastable orthorhombic phase. The interface between orthorhombic VO$_2$ and CoFe$_2$O$_4$ is atomically sharp without noticeable interfacial diffusion. The (010)-faceted orthorhombic VO$_2$ layer is lattice-matched to both the CoFe$_2$O$_4$(111) template and the monoclinic phase, although they have different surface symmetries. The occurrence of an orthorhombic VO$_2$ thin layer significantly lowers the in-plane misfit strains of the monoclinic VO$_2$ epilayer, along both the [100] and [001] axes. Our first-principles calculations confirm that the low-misfit orthorhombic VO$_2$ is preferred on CoFe$_2$O$_4$(111) over the large-misfit monoclinic phase, at the initial growth stage. Additionally, upon increasing the film thickness to ∼8 nm, the orthorhombic phase is no longer favored, and the bulk stable monoclinic VO$_2$ appears to minimize the free energy of the system. Moreover, we show that the metal-to-insulator transition of our VO$_2$ epilayer can be efficiently triggered by both the temperature and Joule self-heating effect.
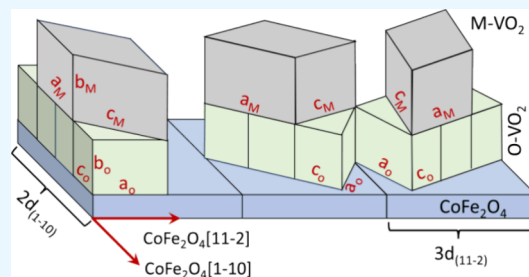
1. INTRODUCTION

As one of the most intensively studied strongly correlated oxides, VO$_2$ is featured by an abrupt metal−insulator transition (MIT) near room temperature (∼340 K), which is accompanied by a monoclinic-to-rutile structural change.[1,2] Such a MIT makes VO$_2$ very attractive for a vast variety of potential applications such as ultrafast switches, smart windows, infrared imaging, Mottronics, and memristors.[3−6] In addition, notable is that the strong coupling among lattice, charge, spin, and orbital degrees of freedom provides additional knobs for manipulating its intrinsic properties and seeking new conceptual devices, through external stimuli including strain, electric and optical fields.[7−10] For instance, both the electrically driven and photoinduced MITs in VO$_2$ have been demonstrated to be fascinating ways to achieve neuromorphic computing for overcoming the limitations of von Neumann architectures.[11,12] In addition, huge piezoresistive response which is an order of magnitude larger than that of silicon was observed in the VO$_2$ nanomembrane, opening the door to the ultrasensitive, low-power-dissipation tactile sensors.[13]

To make these devices reliable and applicable, VO$_2$ epitaxial thin films are highly desirable. However, the growth of device-grade VO$_2$ epitaxial films is challenging. First, it needs a delicate control of the cation valence state, since various vanadium oxides exist including VO, VO$_2$, V$_2$O$_3$, and V$_2$O$_5$, depending on the growth conditions.[14] Second, besides the monoclinic phase, VO$_2$ itself can also exist in several polymorphs.[15] And third, very few isostructural substrates are available for the epitaxial growth of monoclinic VO$_2$ (abbreviated as M-VO$_2$).[16] For example, the most frequently used substrates with two-dimensional surface point symmetry of 3*m* (including 6*mm* symmetry in a more general consideration) are inherently lattice- and symmetry-mismatched with M-VO$_2$.[17] Due to the symmetry mismatch, multiple (010)-oriented M-VO$_2$ domains coexist on the 3*m* substrates, such as Al$_2$O$_3$(0001), ZnO(0001), and (111) facets of perovskite (e.g., SrTiO$_3$), spinel (e.g., MgAl$_2$O$_4$), and rocksalt oxides (e.g., MgO and NiO).[13,16−20] It was reported that on Al$_2$O$_3$(0001) and ZnO(0001) surfaces, the M-VO$_2$ epilayer exhibits a domain-matching epitaxy (LDE) scheme but not the common lattice-matching epitaxy (LME),[13,21] in order to alleviate the considerably huge in-plane epitaxial strain in M-VO$_2$. For instance, a 3 × 3 supercell of M-VO$_2$ matches a 5 × 5 supercell of ZnO when (0001)-faceted ZnO is used as the substrate.[13] By contrast, an interfacial reaction layer (Ni$_2$VO$_4$) appears to guarantee the epitaxial growth of M-VO$_2$,[20] when it is deposited on the NiO(111) surface. Despite the strong influence of misfit strain and surface chemistry, the
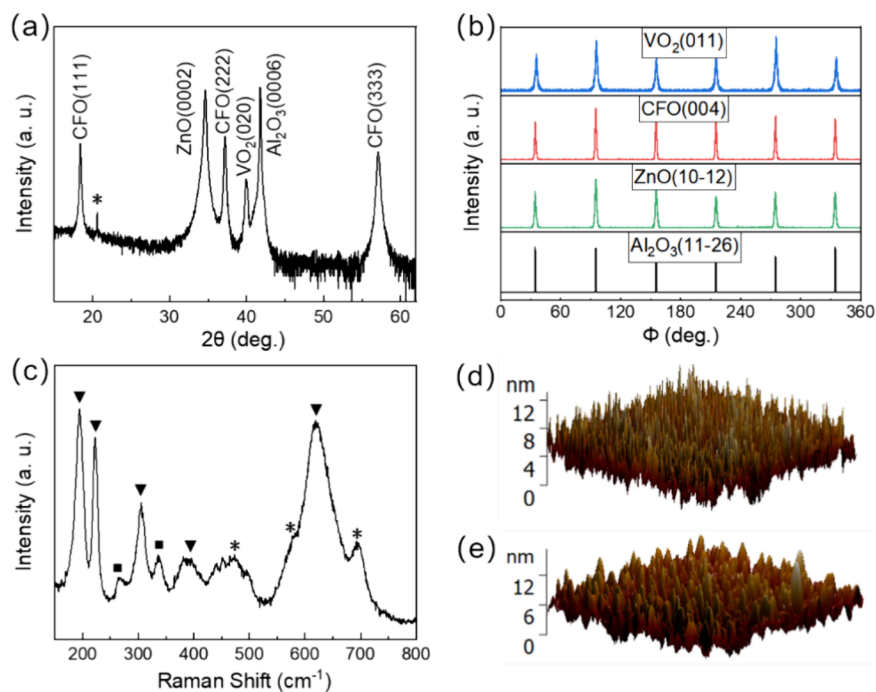
Figure 1. (a) XRD $2\theta-\theta$ pattern of the VO_2 film grown on the CFO/ZnO/Al$_2$O$_3$(0001) substrate. (b) XRD ϕ-scans of VO_2(011), CFO(004), ZnO(10−12), and Al$_2$O$_3$(11−26) reflections. (c) Raman spectrum of VO_2 film; triangles, squares, and stars label the A_g modes, B_g modes, and the signals arising from CoFe$_2$O$_4$. (d,e) Surface morphologies of the CFO template and the VO_2 film; scan area: 2×2 μm^2.

detailed growth mechanism of the M-VO_2 epilayer on $3m$ substrates is far from being understood.

Here, we report the epitaxial growth of M-VO_2 on $3m$ (111)-faceted CoFe$_2$O$_4$ (CFO), through the formation of an interfacial layer of orthorhombic VO_2 (O-VO_2). Direct epitaxy of M-VO_2 on CFO(111) yields anisotropic misfit strains as high as 9.5 and 2.7% along the in-plane [001] and [100] orientations, while the insertion of O-VO_2 thin interfacial layer can significantly accommodate the misfit strains, and therefore makes the epitaxial growth of M-VO_2 possible. Although M-VO_2 is the thermally stable phase, the appearance of metastable O-VO_2 at the interface minimizes the total free energy (E_t) of the whole system through reducing the elastic energy (E_{elas}).

2. EXPERIMENTAL PROCEDURE

2.1. Film Deposition. The VO_2 thin film was fabricated by radio frequency magnetron sputtering with a commercial V$_2$O$_5$ target, on the CFO/ZnO bilayer-buffered Al$_2$O$_3$(0001) substrate. The details of the growth of the CFO/ZnO bilayer were reported before.[22] Prior to the VO_2 deposition, the sputtering chamber was evacuated to a base pressure of 1×10^{-5} Pa, and then filled with the working gas (Ar and O$_2$) to a total pressure of 0.5 Pa. A 10 min presputtering was performed before the growth to avoid any possible contamination. The oxygen partial pressure and substrate temperature were adjusted to be 0.05 Pa and 550 °C during the VO_2 growth, as reported previously.[13]

2.2. Characterization. The X-ray diffraction (XRD) $2\theta-\theta$ and ϕ scans were analyzed by a Rigaku RINT-TTR system using Cu Kα radiation as the light source. A FEI Talos F200S transmission electron microscope (TEM) equipped with an energy-dispersive spectrometer (EDS) was used for the cross-sectional structural and compositional studies. Surface morphologies were characterized by a NT-MDT solver P47 atomic force microscope (AFM) under the noncontact mode.

All of the electrical measurements were carried out using a Keithley-4200 semiconductor characterization system. For characterizing the temperature-dependent resistance of the VO_2 film, a Lakeshore Model 325 controller was used to precisely control the sample temperature. The current−voltage ($I-V$) curve of VO_2 was collected under a current compliance of 0.01A with a contact−contact separation of 20 μm.

2.3. First-Principles Calculations. To derive the elastic energy of M-VO_2(010) and O-VO_2(010) layers under different in-plane strains, first-principles calculations were performed by density functional theory within the projector-augmented waves as implemented in the Vienna Ab initio Simulation Package.[23−25] The electron exchange-correlation potential was described by the Perdew−Burke−Ernzerhof form within the generalized gradient approximation with an on-site Coulomb interaction (GGA + U).[26] The Coulomb parameter U for V-3d orbital states was set to 3.4 eV.[27] For every in-plane strain level, the structures of M-VO_2 and O-VO_2 were optimized such that the remnant Hellmann−Feynman forces were less than 1×10^{-2} eV/Å.

3. RESULTS AND DISCUSSION

Figure 1a shows the $2\theta-\theta$ XRD pattern of the VO_2 film grown on the CFO/ZnO bilayer-buffered Al$_2$O$_3$(0001) substrate. Besides the CFO, ZnO, and substrate-related peaks, a strong M-VO_2(020) peak is observed. The derived out-of-plane parameter is 4.511 Å, similar to those reported previously.[13] In order to disclose the in-plane orientation of M-VO_2 with respect to CFO and the substrate, XRD ϕ-scans were collected along the M-VO_2(011), CFO(004), ZnO(10−12), and Al$_2$O$_3$(11−26) reflections (Figure 1b). It reveals that the VO_2(011) scans exhibit six sharp peaks at 60° intervals, and they appear at azimuthal angles identical to those of CFO(004), ZnO(10−12), and Al$_2$O$_3$(11−26). Therefore, the epitaxial relationships between M-VO_2, CFO, ZnO and the
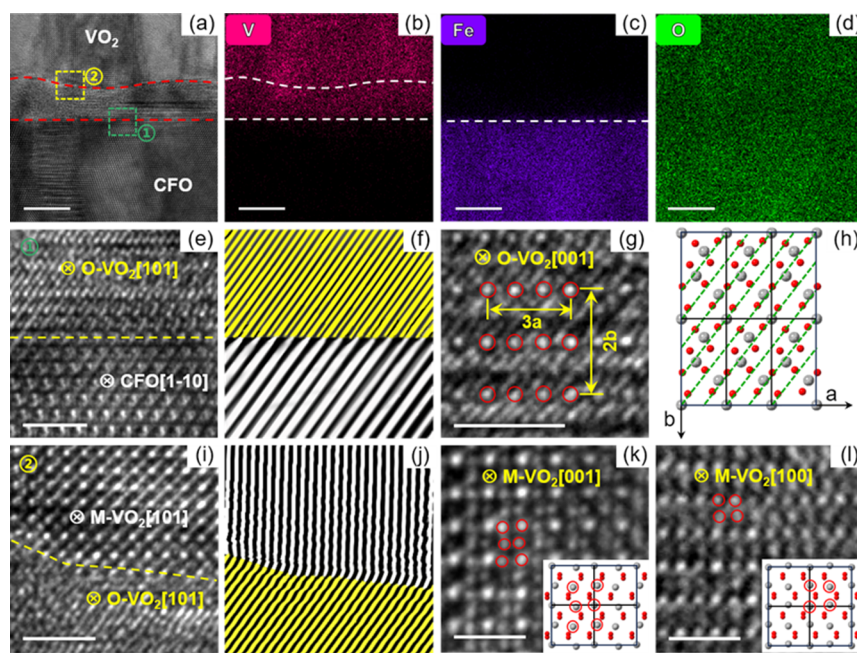
Figure 2. (a) Cross-sectional TEM image near the VO$_2$/CFO interface. (b−d) EDS elemental maps for V, Fe, and O. (e) Enlarged view of the VO$_2$/CFO interfacial region marked by the green square in (a). (f) Reconstructed image obtained by FFT and inverse FFT filtering (e); planes in CFO are shown in white, and the O-VO$_2$ planes are yellow. (g) Cross-sectional image of O-VO$_2$ where the unit cell is clearly resolved. (h) 3 × 2 × 1 supercell of O-VO$_2$ viewed along the [001] axis. (i) Enlarged view of the M-VO$_2$/O-VO$_2$ interfacial region marked by the yellow square in (a). (j) Reconstructed image by FFT and inverse FFT filtering (i); M-VO$_2$ and O-VO$_2$ planes are shown in white and yellow colors, respectively. (k,l) Enlarged views of the regions with zone axes of M-VO$_2$[001] and [100]; insets are supercells of M-VO$_2$ viewed along [001] and [100], respectively. Scale bars are 5 nm in (a−d), 2 nm in (e,g,i), and 1 nm in (k,l).

substrate are determined to be M-VO$_2$[100]∥CFO[1−10]∥ZnO[10−10]∥Al$_2$O$_3$[11−20] and M-VO$_2$(010)∥CFO(111)∥ZnO(0001)∥Al$_2$O$_3$(0001). Similar results were obtained by pole figure characterization (Figure S1). Moreover, strong A_g and B_g modes with peak positions similar to those of M-VO$_2$ reported previously[28] were clearly resolved in the Raman spectrum (Figure 1c), further indicating the deposited VO$_2$ film is of the monoclinic phase. In addition, the VO$_2$ film obtained here has a similar full width at half-maximum (FWHM) of the Raman peaks with the VO$_2$/Al$_2$O$_3$(0001) sample (Figure S2). AFM surface morphology characterizations reveal root-mean-square (RMS) roughnesses of 1.51 and 1.92 nm for the CFO template and the VO$_2$ film (Figure 1d,e), respectively. Note that the RMS roughness obtained here is considerably lower than those of the VO$_2$ epilayers deposited on [LaAlO$_3$]$_{0.3}$[Sr$_2$AlTaO$_6$]$_{0.7}$(111) and SrRuO$_3$-buffered SrTiO$_3$(111)[29,30] and are comparable with the value for the VO$_2$/Al$_2$O$_3$(0001) film (Figure S3).

To gain more insight into the structural details within the interfacial regions between VO$_2$ and the CFO, cross-sectional TEM images were collected along the CFO[1−10] zone axis, as displayed in Figure 2a. Apparently, there occurs a thin (typically ∼8 nm thick) interfacial layer (as denoted by dashed red lines) between M-VO$_2$ and the CFO template, although no XRD signal of this layer is resolvable, partly due to its low volume fraction. In general, there are two possible origins for such a layer: a metastable polymorph of VO$_2$ or a transition metal oxide alloy stemming from an interface chemical reaction. The EDS elemental maps for V, Fe, and O (Figure 2b−d) show that the interface between VO$_2$ and CFO is atomically sharp, without notable interfacial interdiffusion. Therefore, this interfacial layer is mainly composed of V and O and is ascribed to a metastable phase of VO$_2$. Here, it is

identified as O-VO$_2$ (space group: *Pnma*)[31,32] based on the structural details revealed by the enlarged views near the interfacial region (Figure 2e−g). It is found that the O-VO$_2$ layer (zone axis: O-VO$_2$[101]) is semicoherently grown on the CFO template (Figure 2e), and the reconstructed image (Figure 2f) extracted from Figure 2e after fast Fourier transform (FFT) and inverse FFT filtering, clearly shows that one interplane spacing along CFO[002] corresponds to two O-VO$_2$(−1−31) layers. Moreover, the unit cell of O-VO$_2$ can be occasionally resolved in our TEM characterizations, indicating the cooccurrence of the O-VO$_2$[001] zone axis (Figure 2g). In addition, the lattice constants of O-VO$_2$ derived from Figure 2g are in good agreement with those of the orthorhombic phase (JCPDS No. 25-1003).

It is the appearance of a metastable O-VO$_2$ interfacial layer that makes it possible to epitaxially grow M-VO$_2$ on the large-misfit CFO(111) template. We note that an atomically sharp, semicoherent interface between M-VO$_2$ and O-VO$_2$ is also visible, as displayed in Figure 2i, suggesting the high interfacial quality of the M-VO$_2$/O-VO$_2$ system. The reconstructed image derived by FFT and inverse FFT filtering clearly shows that every interplane spacing of M-VO$_2$(20−2) matches well with one O-VO$_2$(−1−31) layer distance (Figure 2j). Besides the M-VO$_2$[101] zone axis (Figure 2i), areas with zone axes of M-VO$_2$[001] and M-VO$_2$[100] are also observed, as illustrated in Figure 2k,l. The finding of 3 different M-VO$_2$ domains confirms the multidomain growth of M-VO$_2$, in accordance with the XRD ϕ-scans as shown in Figure 1b.

In view of the symmetry constraint, the number of domain variants for O-VO$_2$ is 3, when it is epitaxially grown on the 3m CFO(111) surface.[33] That is, 3 equivalent O-VO$_2$ domains coexist on the CFO template (Figure 3), with an in-plane rotation of 120° from each other. The lattice constants of O-
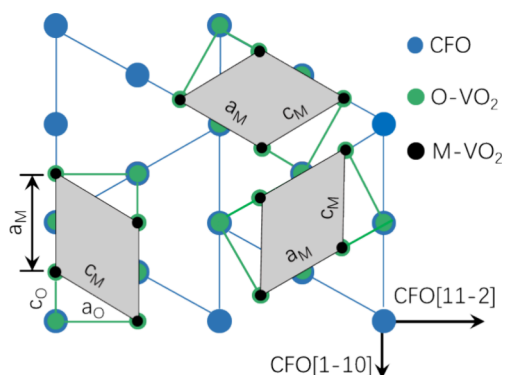
Figure 3. Schematic of the in-plane epitaxial relationship between M-VO$_2$, O-VO$_2$(010), and CFO(111); subscripts "M" and "O" denote the monoclinic and orthorhombic phases, respectively.

VO$_2$ are a = 4.905 Å, b = 9.422 Å, and c = 2.916 Å (JCPDS No. 25-1003), and the resultant lattice misfits between O-VO$_2$ and CFO are 1.04 and 3.91% along O-VO$_2$[001] and [100], respectively.[34] For (111)-oriented CFO film, there are 3 identical <1−10> family of directions, namely, [1−10], [10−1], and [01−1] on the (111) surface. Therefore, the [001] orientations of the 3 O-VO$_2$ domains are parallel with CFO[1−10], [10−1], and [01−1], respectively. The above domain configuration explains why there exist two zone axes of the O-VO$_2$, [001] and [101], in Figure 2e,g. Based on the results shown in Figures 1 and 2, the 3 equivalent M-VO$_2$ domains on the O-VO$_2$ layer are also displayed in Figure 3. According to this domain configuration, the lattice misfits between M-VO$_2$ and O-VO$_2$ are 1.58 and 5.72% along M-VO$_2$[100] and [001], respectively. Based on the above results, the in-plane epitaxial relationship among CFO, O-VO$_2$, and M-VO$_2$ is M-VO$_2$[100]∥O-VO$_2$[001]∥CFO[1−10]. We also note that one single M-VO$_2$ domain shown in Figure 3 stands for a couple of domains with a twisted angle of ∼4° in between, consistent with the observations in (010)-oriented M-VO$_2$ epitaxial films on other 3m substrates reported previously.[13,17,18] This is because the monoclinic distorted angle of M-VO$_2$ is ∼122°, and the couple of twisted domains share the same M-VO$_2$[100] orientation (Figure S4).

We now turn to the underlying mechanism of the appearance of a thin O-VO$_2$ intermediate layer at the VO$_2$/CFO interface. Along the M-VO$_2$[001] and [100] axes, the lattice misfits between M-VO$_2$ and CFO are 8.71 and 2.60%, respectively. By sharp contrast, the lattice misfits between O-VO$_2$ and CFO are hugely reduced to 3.91 and 1.04%, along the [100] and [001] orientations of O-VO$_2$. It seems that the emergence of the O-VO$_2$ layer alleviates the epitaxial strain and, therefore, reduces the total free energy E_t of the whole system. In order to verify this viewpoint, first-principles calculations were performed to derive E_t of the O-VO$_2$ and M-VO$_2$ epilayers as functions of in-plane strains, as shown in Figure 4. Generally, E_t is the sum of the elastic energy E_{elas} arising from strain-induced lattice distortion and the free energy under the strain-free state (E_0).[35] According to our calculations, E_0 for the strain-free M-VO$_2$ is 0.132 eV lower than that of unstrained O-VO$_2$ per formula unit (f.u.). Here, for convenience, we set the E_0 of unstrained M-VO$_2$ as zero in Figure 4.

For the fully strained O-VO$_2$ on CFO(111) (solid star in Figure 4b), we get E_t = 0.147 eV/f.u. By comparison, E_t is as high as 0.269 eV/f.u. (solid circle in Figure 4d) when M-VO$_2$ is
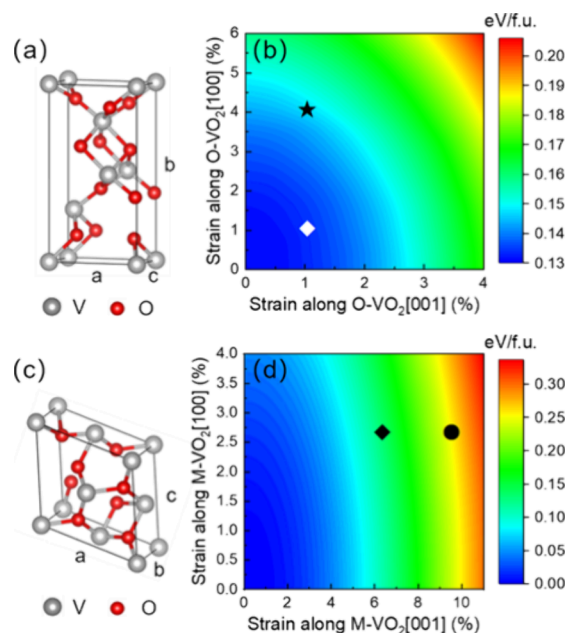

Figure 4. (a) Schematic of the unit cell of the O-VO$_2$. (b) Total energy of O-VO$_2$ as functions of strains along O-VO$_2$[100] and [001] orientations; black stars denote the coherent O-VO$_2$(010) epilayer on CFO(111), and the white diamond labels the strain level of O-VO$_2$ where the total energy of O-VO$_2$ is equal to that of the M-VO$_2$ coherent epilayer on O-VO$_2$. (c) Schematic of the M-VO$_2$ unit cell. (d) Total energy of M-VO$_2$ as functions of strains along M-VO$_2$[100] and [001] directions; black spots stars denote the coherent M-VO$_2$(010) epilayer on CFO(111), and the black diamond labels the strain level of M-VO$_2$ where the M-VO$_2$ epilayer starts to appear.

coherently strained on CFO(111). In this regard, the energy of O-VO$_2$ is energetically more favorable than that of M-VO$_2$ at the initial growth stage. In general, a strained epilayer gradually relaxes toward its bulk state, upon increasing the film thickness above the critical thickness.[36] For our O-VO$_2$ epilayer coherently strained on CFO(111), the structural relaxation is somewhat different from that of the conventional isotropically strained film. The rather large strain (4.07%) applied along the O-VO$_2$[100] direction yields a considerably low critical thickness and, at the initial relaxation period, the strain (1.05%) across the direction of the O-VO$_2$[001] can be viewed as a constant (Figure S5). When this anisotropic relaxation proceeds and the strain along O-VO$_2$[100] reaches 1.03% (the white diamond in Figure 4b), another relaxation route—the O-to-M phase transition, appears. According to our calculations, the diamond spots (white in Figure 4b and black in Figure 4d) infer the strain levels at which O-VO$_2$ and M-VO$_2$ are coherent with each other and share the same E_t. Our experimental observations (Figure 2a) show that the O-to-M phase transition occurs at a threshold thickness of ∼8 nm for O-VO$_2$; beyond that thickness, M-VO$_2$ is energetically preferred over M-VO$_2$. As compared with the coherent M-VO$_2$ epilayer directly appears on CFO(111), both the strain level and E_{elas} of M-VO$_2$ (the black diamond in Figure 4d) fully strained on the partially relaxed O-VO$_2$ (the white diamond in Figure 4b) are hugely reduced. Moreover, the threshold strain level below which the formation of the O-VO$_2$ interfacial layer is no more energetically favorable on the 3m substrate can also be derived based on our calculations (Figure S6).

It is worth pointing out that besides the strain level, film thickness is also a key parameter to tailor the energy balance

between competing polymorphs as well as to control the detailed structure of the film. For an epilayer of a metastable phase, only a limited thickness is allowed. In order to minimize E_t of the whole system, a strain-driven metastable polymorph inherently tends to turn into its parent phase upon increasing the film thickness to a threshold value, as exemplified by the orthorhombic-to-monoclinic transition found here. Similar thickness-dependent structural evolutions have been observed in a variety of systems, including tetragonal $BiFeO_3$ and orthorhombic $Hf_{0.5}Zr_{0.5}O_2$ epitaxial thin films.[37,38]

We carried out temperature-dependent resistance characterizations for the VO_2 film deposited on the CFO(111) template (Figure 5a), and a MIT characterized by a resistance variation
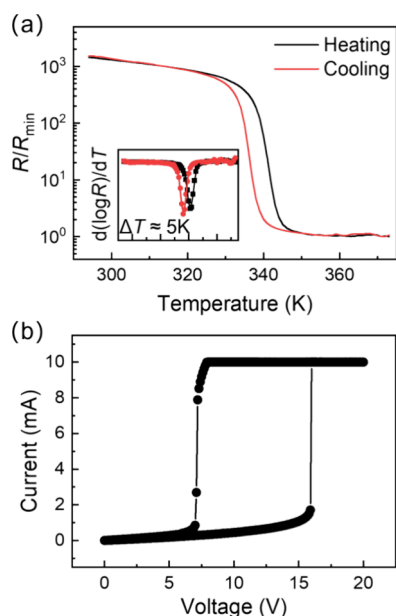
Figure 5. (a) Normalized resistance versus temperature; inset is the derivative curve of log $R(T)-T$ plots, in which T_c and ΔT are derived from the Gaussian fit of the data. (b) $I-V$ characterization of the VO_2 film collected under a contact−contact separation of 20 μm with a current compliance of 0.01 A.

of ∼3 orders of magnitude was observed. The MIT temperature (T_c), defined as the peak position in the derivative of the $R(T)$, is ∼341 K during heating, close to the bulk value of M-VO_2.[39] Moreover, the phase transition sharpness (ΔT, ∼5 K) also resembles those of the VO_2 epitaxial films grown on other $3m$ substrates.[13] Besides temperature, the MIT of VO_2 can also be driven by electric field through the Joule self-heating effect.[40,41] As shown in Figure 5b, the $I-V$ curve is highly nonlinear—I increases gradually with V at the beginning of the voltage sweep; it abruptly jumps from 1.7 to 10.0 mA as V rises to 15.9 V, indicating the occurrence of a monoclinic-to-rutile phase transition. Upon decreasing the temperature, a large hysteresis (ΔV = 8.7 V) appears and the VO_2 film transforms back to the insulator state at V = 7.2 V. All these findings are similar to those reported previously,[13] indicating a high electrical quality of the VO_2 film on CFO(111) which has important implications for device applications.

4. CONCLUSIONS

In summary, we have demonstrated the heteroepitaxy of a VO_2 thin film with good structural and electrical qualities, on the large-misfit $3m$ CFO(111) template. Cross-sectional TEM

characterizations show that the interface between VO_2 and the CFO is reasonably good, without any notable interlayer diffusion. In addition, it is found that a metastable O-VO_2 thin layer appears at the interface, with 3 domain variants on CFO(111). The occurrence of an O-VO_2 interfacial layer, with the in-plane epitaxial relationship of M-$VO_2[100]\|$O-$VO_2[001]\|$CFO$[1-10]$, significantly reduces the lattice mismatch of the VO_2/CFO system. Based on first-principles calculations, the total free energies of M-VO_2 and O-VO_2 epilayers with respect to the in-plane anisotropic misfit strains were derived. The results explain why O-VO_2 but not the thermally stable M-VO_2 emerges on CFO(111) at the initial growth stage and clarify the origin of the O-to-M structural relaxation route. Our work provides an in-depth understanding on the epitaxial growth of VO_2 on $3m$ surface, which is beneficial for its future applications.

■ ASSOCIATED CONTENT

Ⓢ Supporting Information

The Supporting Information is available free of charge at https://pubs.acs.org/doi/10.1021/acsomega.4c03810.

Pole figure characterizations of the VO_2 film on the CFO template, comparison of the Raman spectra for the films grown on CFO and $Al_2O_3(0001)$, surface morphology of the VO_2 film grown on $Al_2O_3(0001)$, XRD ϕ-scans of $VO_2(220)$ and the schematic of twisted domain couple, the dependence of critical thickness on the in-plane strain according to the People-Bean model, and the derivation of the threshold strain level for the occurrence of interfacial O-VO_2 on $3m$ substrate (PDF)

■ AUTHOR INFORMATION

Corresponding Authors

Xingxing Li − *School of Electronic and Information Engineering, Wuyi University, Jiangmen 529020 Guangdong, China*; Email: wyuxxli@163.com

Zhigang Yin − *Key Lab of Semiconductor Materials Science, Institute of Semiconductors, Chinese Academy of Sciences, Beijing 100083, China; Center of Materials Science and Optoelectronics Engineering, University of Chinese Academy of Sciences, Beijing 100049, China;* ⓘ orcid.org/0000-0002-8385-7055; Email: yzhg@semi.ac.cn

Authors

Zhiwei Zhang − *School of Electronic and Information Engineering, Wuyi University, Jiangmen 529020 Guangdong, China; Key Lab of Semiconductor Materials Science, Institute of Semiconductors, Chinese Academy of Sciences, Beijing 100083, China*

Yong Cheng − *Key Lab of Semiconductor Materials Science, Institute of Semiconductors, Chinese Academy of Sciences, Beijing 100083, China; Center of Materials Science and Optoelectronics Engineering, University of Chinese Academy of Sciences, Beijing 100049, China*

Bo Li − *Key Lab of Semiconductor Materials Science, Institute of Semiconductors, Chinese Academy of Sciences, Beijing 100083, China; Center of Materials Science and Optoelectronics Engineering, University of Chinese Academy of Sciences, Beijing 100049, China*

Jinliang Wu − *Key Lab of Semiconductor Materials Science, Institute of Semiconductors, Chinese Academy of Sciences, Beijing 100083, China*

Ling Zhang − *Key Lab of Semiconductor Materials Science, Institute of Semiconductors, Chinese Academy of Sciences, Beijing 100083, China;* orcid.org/0000-0003-4207-5724

Xingwang Zhang − *Key Lab of Semiconductor Materials Science, Institute of Semiconductors, Chinese Academy of Sciences, Beijing 100083, China; Center of Materials Science and Optoelectronics Engineering, University of Chinese Academy of Sciences, Beijing 100049, China;* orcid.org/0000-0001-7873-5566

Complete contact information is available at:
https://pubs.acs.org/10.1021/acsomega.4c03810

Author Contributions

The manuscript was written through the contributions of all authors. All authors have given approval to the final version of the manuscript.

Notes

The authors declare no competing financial interest.

■ REFERENCES

(1) Morin, F. J. Oxides Which Show a Metal-to-Insulator Transition at the Neel Temperature. *Phys. Rev. Lett.* **1959**, *3*, 34−36.

(2) Aetukuri, N. B.; Gray, A. X.; Drouard, M.; Cossale, M.; Gao, L.; Reid, A. H.; Kukreja, R.; Ohldag, H.; Jenkins, C. A.; Arenholz, E.; Roche, K. P.; Dürr, H. A.; Samant, M. G.; Parkin, S. S. P. Control of the Metal-Insulator Transition in Vanadium Dioxide by Modifying Orbital Occupancy. *Nat. Phys.* **2013**, *9*, 661−666.

(3) Nakano, M.; Shibuya, K.; Okuyama, D.; Hatano, T.; Ono, S.; Kawasaki, M.; Iwasa, Y.; Tokura, Y. Collective Bulk Carrier Delocalization Driven by Electrostatic Surface Charge Accumulation. *Nature* **2012**, *487*, 459−462.

(4) Yi, W.; Tsang, K. K.; Lam, S. K.; Bai, X.; Crowell, J. A.; Flores, E. A. Biological Plausibility and Stochasticity in Scalable VO2 Active Memristor Neurons. *Nat. Commun.* **2018**, *9*, 4661.

(5) Shukla, N.; Parihar, A.; Freeman, E.; Paik, H.; Stone, G.; Narayanan, V.; Wen, H.; Cai, Z.; Gopalan, V.; Engel-Herbert, R.; Schlom, D. G.; Raychowdhury, A.; Datta, S. Synchronized Charge Oscillations in Correlated Electron Systems. *Sci. Rep.* **2014**, *4*, 4964.

(6) Zhou, X.; Shang, Y.; Gu, Z.; Jiang, G.; Ozawa, T.; Mao, W.; Fukutani, K.; Matsuzaki, H.; Jiang, Y.; Chen, N.; Chen, J. Revealing the Role of High-Valence Elementary Substitution in the Hydrogen-Induced Mottronic Transitions of Vanadium Dioxide. *Appl. Phys. Lett.* **2024**, *124*, No. 082103.

(7) Fan, L. L.; Chen, S.; Luo, Z. L.; Liu, Q. H.; Wu, Y. F.; Song, L.; Ji, D. X.; Wang, P.; Chu, W. S.; Gao, C.; Zou, C. W.; Wu, Z. Y. Strain Dynamics of Ultrathin VO2 Film Grown on TiO2 (001) and the Associated Phase Transition Modulation. *Nano Lett.* **2014**, *14*, 4036−4043.

(8) Lee, Y. J.; Hong, K.; Na, K.; Yang, J.; Lee, T. H.; Kim, B.; Bark, C. W.; Kim, J. Y.; Park, S. H.; Lee, S.; Jang, H. W. Nonvolatile Control of Metal-Insulator Transition in VO2 by Ferroelectric Gating. *Adv. Mater.* **2022**, *34*, No. 2203097.

(9) Li, J.; Wu, L.; Yang, S.; Jin, X.; Wang, W.; Tao, J.; Boatner, L.; Babzien, M.; Fedurin, M.; Palmer, M.; Yin, W.; Delaire, O.; Zhu, Y. Direct Detection of V-V Atom Dimerization and Rotation Dynamic Pathways upon Ultrafast Photoexcitation in VO2. *Phys. Rev. X* **2022**, *12*, No. 021032.

(10) Morrison, V. R.; Chatelain, R. P.; Tiwari, K. L.; Hendaoui, A.; Bruhács, A.; Chaker, M.; Siwick, B. J. A Photoinduced Metal-like Phase of Monoclinic VO2 Revealed by Ultrafast Electron Diffraction. *Science* **2014**, *346*, 445−448.

(11) Li, G.; Xie, D.; Zhong, H.; Zhang, Z.; Fu, X.; Zhou, Q.; Li, Q.; Ni, H.; Wang, J.; Guo, E.-j.; He, M.; Wang, C.; Yang, G.; Jin, K.; Ge, C. Photo-Induced Non-Volatile VO2 Phase Transition for Neuromorphic Ultraviolet Sensors. *Nat. Commun.* **2022**, *13*, 1729.

(12) Schofield, P.; Bradicich, A.; Gurrola, R. M.; Zhang, Y.; Brown, T. D.; Pharr, M.; Shamberger, P. J.; Banerjee, S. Harnessing the Metal-Insulator Transition of VO2 in Neuromorphic Computing. *Adv. Mater.* **2023**, *35*, No. 2205294.

(13) Li, X.; Yin, Z.; Zhang, X.; Wang, Y.; Wang, D.; Gao, M.; Meng, J.; Wu, J.; You, J. Epitaxial Liftoff of Wafer-Scale VO2 Nanomembranes for Flexible, Ultrasensitive Tactile Sensors. *Adv. Mater. Technol.* **2019**, *4*, No. 1800695.

(14) Kumar, M.; Lim, S.; Kim, J.; Seo, H. Picoampere Dark Current and Electro-Opto-Coupled Sub-to-Super-linear Response from Mott-Transition Enabled Infrared Photodetector for Near-Sensor Vision Processing. *Adv. Mater.* **2023**, *35*, No. 2210907.

(15) Lee, S.; Ivanov, I. N.; Keum, J. K.; Lee, H. N. Epitaxial Stabilization and Phase Instability of VO2 Polymorphs. *Sci. Rep.* **2016**, *6*, 19621.

(16) Lu, J.; West, K. G.; Wolf, S. A. Very Large Anisotropy in the DC Donductivity of Epitaxial VO2 Thin Films Grown on (011) Rutile TiO2 Substrates. *Appl. Phys. Lett.* **2008**, *93*, No. 262107.

(17) Wong, F. J.; Zhou, Y.; Ramanathan, S. Epitaxial Variants of VO2 Thin Films on Complex Oxide Single Crystal Substrates with 3m Surface Symmetry. *J. Cryst. Growth* **2013**, *364*, 74−80.

(18) Diebold, L.; Maroutian, T.; Largeau, L.; Guiblin, N.; Bude, R.; Garry, G.; Ishchenko, O. M.; Aubert, P. Impact of the Crystallographic Variants of VO2 Thin Films on c- and r-Cut Sapphire on Structural Phase Transition and Radiofrequency Properties. *Appl. Phys. Lett.* **2023**, *123*, No. 131601.

(19) John, J.; Slassi, A.; Sun, J.; Sun, Y.; Bachelet, R.; Pénuelas, J.; Saint-Girons, G.; Orobtchouk, R.; Ramanathan, S.; Calzolari, A.; Cueff, S. Tunable Optical Anisotropy in Epitaxial Phase-Change VO2 Thin Films. *Nanophotonics* **2022**, *11*, 3913−3922.

(20) Moatti, A.; Sachan, R.; Narayan, J. Mechanism of Strain Relaxation: Key to Control of Structural and Electronic Transitions in VO2 Thin-Films. *Mater. Res. Lett.* **2020**, *8*, 16−22.

(21) McGee, R.; Goswami, A.; Pal, S.; Schofield, K.; Bukhari, S. A. M.; Thundat, T. Sharpness and Intensity Modulation of the Metal-Insulator Transition in Ultrathin VO2 Films by Interfacial Structure Manipulation. *Phys. Rev. Mater.* **2018**, *2*, No. 034605.

(22) Jiang, Y.; Li, X.; Zhang, X.; Cheng, Y.; Zhang, L.; Dong, H.; Yin, Z.; Zhang, X. Absence of Auxeticity in CoFe2O4 Epitaxial Films. *Jpn. J. Appl. Phys.* **2022**, *61*, No. 070901.

(23) Blöchl, P. E. Projector Augmented-Wave Method. *Phys. Rev. B* **1994**, *50*, 17953−17979.

(24) Kresse, G.; Joubert, D. From Ultrasoft Pseudopotentials to the Projector Augmented-Wave Method. *Phys. Rev. B* **1999**, *59*, 1758−1775.

(25) Kresse, G.; Furthmüller, J. Efficient Iterative Schemes for ab initio Total-Energy Calculations Using a Plane-Wave Basis Set. *Phys. Rev. B* **1996**, *54*, 11169−11186.

(26) Perdew, J. P.; Burke, K.; Ernzerhof, M. Generalized Gradient Approximation Made Simple. *Phys. Rev. Lett.* **1996**, *77*, 3865−3868.

(27) Chen, L.; Wang, X.; Shi, S.; Cui, Y.; Luo, H.; Gao, Y. Tuning the Work Function of VO2(100) Surface by Ag Adsorption and Incorporation: Insights from First-Principles Calculations. *Appl. Surf. Sci.* **2016**, *367*, 507−517.

(28) Kim, H.-T.; Chae, B.-G.; Youn, D.-H.; Kim, G.; Kang, K.-Y.; Lee, S.-J.; Kim, K.; Lim, Y.-S. Raman Study of Electric-Field-Induced First-Order Metal-Insulator Transition in VO2-Based Devices. *Appl. Phys. Lett.* **2005**, *86*, No. 242101.

(29) Liu, Y.; Niu, S.; Orvis, T.; Zhang, H.; Zhao, H.; Wang, H.; Ravichandran, J. Epitaxial Growth and Electrical Properties of VO2 on [LaAlO3]0.3[Sr2AlTaO6]0.7(111) Substrate. *J. Vac. Sci. Technol. A* **2018**, *36*, No. 061506.

(30) Zhang, C.; Bisht, R. S.; Nozariasbmarz, A.; Saha, A.; Han, C. S.; Wang, Q.; Yuan, Y.; Sengupta, A.; Priya, S.; Ramanathan, S. Synthesis

and Electrical Behavior of VO$_2$ Thin Films Grown on SrRuO$_3$ Electrode Layers. *J. Vac Sci. Technol. A* **2022**, *40*, No. 043405.

(31) Wu, C.; Hu, Z.; Wang, W.; Zhang, M.; Yang, J.; Xie, Y. Synthetic Paramontroseite VO$_2$ with Good Aqueous Lithium−ion Battery Performance. *Chem. Commun.* **2008**, *33*, 3891−3893.

(32) Braham, E. J.; Andrews, J. L.; Alivio, T. E. G.; Fleer, N. A.; Banerjee, S. Stabilization of a Metastable Tunnel-Structured Orthorhombic Phase of VO$_2$ upon Iridium Doping. *Phys. Status Solidi A* **2018**, *215*, No. 1700884.

(33) Grundmann, M. Formation of Epitaxial Domains: Unified Theory and Survey of Experimental Results. *Phys. Stat. Sol. (b)* **2011**, *248*, 805−824.

(34) For convenience, here the lattice misfit is defined as |$(a_{film} − a_{sub})/a_{sub}$|. For the coherent epitaxy, $(a_{sub} − a_{film})/a_{film}$ is termed as the lattice misfit strain; the positive and negative signs indicate compressive and tensile in-plane strains, respectively.

(35) Zhao, Y.; Yin, Z.; Li, X.; Zheng, M.; Cheng, Y.; You, J.; Wu, J.; Zhang, X. Metastable Tetragonal BiFeO$_3$ Stabilized on Anisotropic a-Plane ZnO. *Cryst. Growth Des.* **2021**, *21*, 4372−4379.

(36) People, R.; Bean, J. C. Calculation of Critical Layer Thickness Versus Lattice Mismatch for Ge$_x$Si$_{1−x}$/Si Strained-Layer Hetero-structures. *Appl. Phys. Lett.* **1985**, *47*, 322−324.

(37) Zeches, R. J.; Rossell, M. D.; Zhang, J. X.; Hatt, A. J.; He, Q.; Yang, C. H.; Kumar, A.; Wang, C. H.; Melville, A.; Adamo, C.; Sheng, G.; Chu, Y. H.; Ihlefeld, J. F.; Erni, R.; Ederer, C.; Gopalan, V.; Chen, L. Q.; Schlom, D. G.; Spaldin, N. A.; Martin, L. W.; Ramesh, R. A Strain-Driven Morphotropic Phase Boundary in BiFeO$_3$. *Science* **2009**, *326*, 977−980.

(38) Zhang, Z.; Hsu, S.-L.; Stoica, V. A.; Paik, H.; Parsonnet, E.; Qualls, A.; Wang, J.; Xie, L.; Kumari, M.; Das, S.; Leng, Z.; McBriarty, M.; Proksch, R.; Gruverman, A.; Schlom, D. G.; Chen, L.-Q.; Salahuddin, S.; Martin, L. W.; Ramesh, R. Epitaxial Ferroelectric Hf$_{0.5}$Zr$_{0.5}$O$_2$ with Metallic Pyrochlore Oxide Electrodes. *Adv. Mater.* **2021**, *33*, No. 2006089.

(39) Mun, B. S.; Chen, K.; Yoon, J.; Dejoie, C.; Tamura, N.; Kunz, M.; Liu, Z.; Grass, M. E.; Mo, S.-K.; Park, C.; Lee, Y. Y.; Ju, H. Nonpercolative Metal-Insulator Transition in VO$_2$ Single Crystals. *Phys. Rev. B* **2011**, *84*, No. 113109.

(40) Bae, S.-H.; Lee, S.; Koo, H.; Lin, L.; Jo, B. H.; Park, C.; Wang, Z. L. The Memristive Properties of a Single VO$_2$ Nanowire with Switching Controlled by Self-Heating. *Adv. Mater.* **2013**, *25*, 5098−5103.

(41) Liu, Y.; Liu, A.; Chai, X.; Yang, Y.; Lu, M.; Bai, X.; Chen, Y.; Zhang, Y. An Interesting Functional Phase Change Material VO$_2$: Response to Multivariate Control and Extensive Applications in Optics and Electronics. *Adv. Electron. Mater.* **2024**, *10*, No. 2300699.